Highly Electrocatalytic Activity of RuO$_2$ Nanocrystals for Triiodide Reduction in Dye-Sensitized Solar Cells

Yu Hou, Zu Peng Chen, Dong Wang, Bo Zhang, Shuang Yang, Hai Feng Wang,* P. Hu, Hui Jun Zhao, and Hua Gui Yang*

Dye-sensitized solar cells (DSCs) are promising alternatives to conventional silicon devices because of their simple fabrication procedure, low cost, and high efficiency. Platinum is generally used as a superior counter electrode (CE) material, but the disadvantages such as high cost and low abundance greatly restrict the large-scale application of DSCs. An efficient and sustainable way to overcome the limited supply of Pt is the development of high-efficiency Pt-free CE materials, which should possess both high electrical conductivity and superior electrocatalytic activity simultaneously. Herein, for the first time, a two-step strategy to synthesize ruthenium dioxide (RuO$_2$) nanocrystals is reported, and it is shown that RuO$_2$ catalysts exhibit promising electrocatalytic activity towards triiodide reduction, which results in comparable energy conversion efficiency to that of conventional Pt CEs. More importantly, by virtue of first-principles calculations, the catalytic mechanism of electrocatalysis for triiodide reduction on various CEs is investigated systematically and it is found that the electrochemical triiodide reduction reaction on RuO$_2$ catalyst surfaces can be enhanced significantly, owing to the ideal combination of good electrocatalytic activity and high electrical conductivity.

1. Introduction

The generation of electrical power by solar energy conversion is an attractive and sustainable solution to the energy problem. Dye-sensitized solar cells (DSCs) have stood out among various photovoltaic devices and have attracted a great deal of interest owing to their low cost, simple fabrication procedure, environmental friendliness, and relatively

Y. Hou, Z. P. Chen, Dr. B. Zhang, S. Yang, Prof. H. G. Yang
Key Laboratory for Ultrafine Materials of Ministry of Education
School of Materials Science and Engineering
East China University of Science and Technology
130 Meilong Road, Shanghai 200237, China
E-mail: hgyang@ecust.edu.cn

D. Wang, Dr. H. F. Wang, Prof. P. Hu
State Key Laboratory of Chemical Engineering
Centre for Computational Chemistry and Research Institute
of Industrial Catalysis
East China University of Science and Technology
130 Meilong Road, Shanghai 200237, China
E-mail: hfwang@ecust.edu.cn

Dr. B. Zhang
Department of Physics
East China University of Science and Technology
130 Meilong Road, Shanghai 200237, China

Prof. P. Hu
School of Chemistry and Chemical Engineering
The Queen's University of Belfast
Belfast BT9 5AG, UK

Prof. H. J. Zhao, Prof. H. G. Yang
Centre for Clean Environment and Energy
Gold Coast Campus
Griffith University
Queensland 4222, Australia

high efficiency, which make them promising candidates for the next generation of solar cells.[1–5] As an important component of DSCs, the counter electrode (CE) catalyzes the reduction of triiodide to iodide and collects electrons from the external circuit. In the development of DSCs, platinum (Pt) was commonly considered as a superior CE material with excellent catalytic activity and high electrical conductivity. However, the limited reserves and high cost of Pt severely restrict the large-scale application of DSCs.[6–8] So far, considerable efforts have been made to develop high-efficiency substitutes for Pt, such as carbon materials and conductive organic polymers,[9–12] but their stabilities and catalytic activities are not satisfactory. Some inorganic semiconductor materials have also been explored as CEs in DSCs, including metal sulfides,[13,14] metal nitrides,[15,16] metal carbides,[17] metal oxides,[18,19] metal selenides,[20] and copper zinc tin sulfide.[7] Recently, our group developed a general and efficient screening strategy for the electrocatalytic activity of CEs and successfully used α-Fe₂O₃ as a new CE catalyst, which demonstrates promising electrocatalytic activity towards triiodide reduction at a rate comparable to that of Pt.[18] However, it is usually not easy to meet both the high electrical conductivity and superior electrocatalytic activity for metal oxides simultaneously, which play crucial roles in determining the performance of DSCs. Moreover, the mechanism in affecting the electrocatalytic activity of triiodide reduction on the electrode surface has not been fully understood to date.

It has been reported that ruthenium dioxide (RuO₂) exhibits superior electrocatalytic activities and it has been widely applied in heterogeneous catalysis including oxidation reactions, reduction/hydrogenation reactions, and ammonia synthesis. Furthermore, RuO₂ has also been exploited in dynamic random-access memory (DRAM) capacitors and lithium-ion batteries owing to its high conductivity.[21,22] With respect to the triiodide reduction reaction, in the strategy proposed previously to screen CE materials,[18] the adsorption energy of the I atom (E_{ad}^I) at the acetonitrile/electrode interface was suggested to be a good descriptor and the materials with E_{ad}^I ranging from around 0.33 to 1.20 eV were predicted to be usually catalytically active electrodes.[18] Within the density functional theory (DFT) framework, the adsorption energy of the I atom at the interface of acetonitrile/RuO₂ was calculated to be within this range (0.59 eV), which is almost identical to that at the acetonitrile/Pt(111) interface (0.52 eV).[18] RuO₂ is therefore expected to be catalytically active. Based on this theoretical prediction, we have proposed a new two-step strategy to synthesize RuO₂ catalysts, which were used as the CE material in DSCs, and found that RuO₂ can reach the same level of energy conversion efficiency (7.22%) as the traditional Pt DSC (7.17%) resulting from the simultaneous superior electrocatalytic activity and high electrical conductivity. More importantly, an in-depth understanding of the catalytic mechanism of triiodide reduction on the RuO₂ CEs has been carried out by using first-principles calculations, which confirmed that the electrochemical triiodide reduction reaction on RuO₂ catalyst surfaces can be enhanced relative to the Pt CE.

2. Results and Discussion

2.1. Iodine Reduction Reaction (IRR) on RuO₂(110)

To further estimate the catalytic activity of RuO₂ nanocrystals, a molecular-level investigation into the triiodide reduction reaction at the CH₃CN/RuO₂(110) interface was conducted by virtue of DFT calculations. As demonstrated previously,[18,23] the mechanism of triiodide reduction (I_3^-(sol) + 2e⁻ → 3I⁻(sol)) could usually be described as follows:

$$I_3^-(sol) \leftrightarrow I_2(sol) + I^-(sol) \tag{1}$$

$$I_2(sol) + 2* \rightarrow 2I* \tag{2}$$

$$I* + e^- \rightarrow I^-(sol) \tag{3}$$

where * represents the free site on the electrode surface and sol indicates the acetonitrile solution. Since the solution reaction (I_3^-(sol) ↔ I_2(sol) + I⁻(sol)) was verified to be usually fast and regarded as being in equilibrium,[23] the overall catalytic activity would therefore be determined by the molecular IRR (I_2(sol) + 2e⁻ → 2I⁻(sol)) occurring at the liquid/solid interface, which consists of I₂ dissociation (step 2) and I* desorption resulting from one-electron reduction (step 3). Hence, we focused on these two elementary reaction steps at the CH₃CN/RuO₂(110) interface.

The lattice parameters of rutile-structured bulk RuO₂ were optimized to be a = 4.515 and c = 3.123 Å, as shown in **Figure 1**a, which agrees well with the experimental values (a = 4.492 and c = 3.107 Å). From Figure 1b, one can see that the RuO₂(110) surface presents exposed rows of five-coordinated Ru cations (Ru₅c) and lattice oxygen atoms (two- or three-coordinated; O₂c or O₃c), in which these coordinately unsaturated Ru₅c constitute the typical catalytically active sites.[24] On the Ru₅c row, it is found from the DFT results that the iodine molecule (I₂) would readily dissociate into two I* atoms upon adsorption without an obvious dissociation barrier, which is similar to the situation at the CH₃CN/Pt(111) interface.[18] The formed I* atoms preferably sit on top of the surface Ru₅c atom at a distance, d (Ru–I), of 2.84 Å (see Figure 1c). The charge density differences are illustrated to show the bond properties between I and the surface Ru₅c atom at this adsorption configuration. As shown in Figure 1c, accompanying the adsorption of the I atom, electrons accumulate at I* resulting from the electron depletion at the surface Ru₅c, as well as the surface-adsorbed CH₃CN molecules and the nearest surface O₂c, and Ru–I interaction assumes a sort of polar covalent bond. The adsorption energy of the I* atom was calculated to be 0.59 eV relative to half an I₂ molecule in the gas phase, which is a little stronger than that on the Pt electrode surface (0.52 eV).[18] Subsequently, the adsorbed I* atom can receive one electron and then desorb into solution in the form of I⁻ with a much elongated Ru–I bond at the transition state (TS, 4.16 Å, see Figure 1d). From Figure 1e, one can see that at the TS, the I atom is surrounded by CH₃CN molecules and is stabilized owing to the Coulomb attraction from H–I interaction and repulsion from the N end of the surface-adsorbed CH₃CN molecule. The corresponding desorption barrier (E_a^{des}) was calculated to be
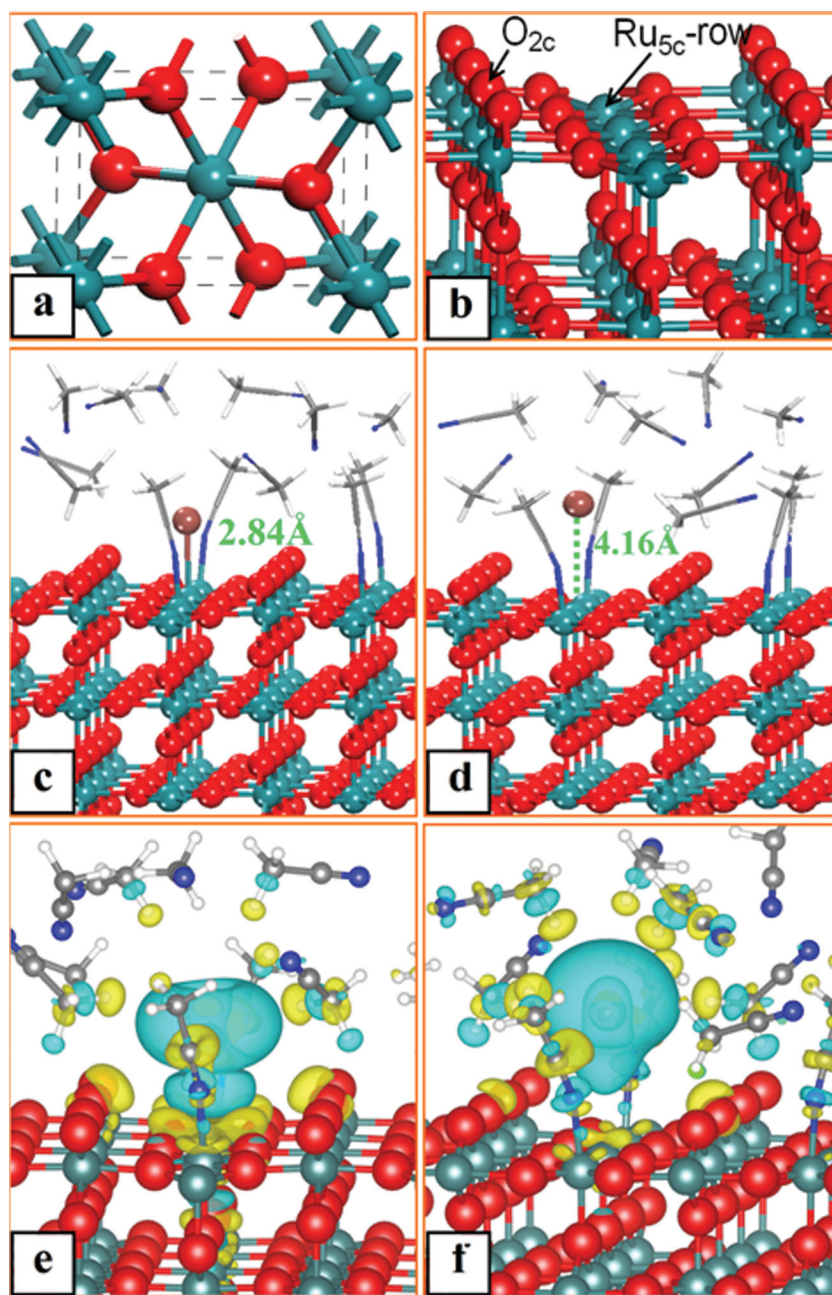
Figure 1. Geometric and electronic structures of key intermediates and Gibbs free energy profile of IRR. a) Atomic configuration of bulk RuO_2. b) The $RuO_2(110)$ surface, which mainly exposes five-coordinated Ru_{5c} and two-/three-coordinated lattice oxygen atoms. c) Adsorption configuration of I at the $CH_3CN/RuO_2(110)$ interface. d) TS structure of I* desorption resulting from one-electron reduction. e,f) The 3D isosurface (at an isovalue of 0.005) of the charge density difference for the I* adsorption structure and desorption TS structure, respectively. Red: oxygen; green: ruthenium; blue: nitrogen; gray: carbon; white: hydrogen.

analysis indicates that more electrons flow into the p-orbitalorbital of the I atom at the TS, with a charge of 0.46 and 0.65 e for I species at the I adsorption state and TS, respectively.

2.2. Synthesis Procedure

To verify these theoretical predictions, phase-pure RuO_2 nanocrystals were synthesized by a novel two-step method. Firstly, the amorphous $RuO_2 \cdot nH_2O$ intermediate was prepared by a facile hydrothermal process using ruthenium(III) chloride hydrate ($RuCl_3 \cdot xH_2O$) and sodium hydroxide (NaOH) as the precursor and the reaction-controlling agent, respectively, which were kept in a Teflon-lined stainless-steel autoclave at 180 °C for 48 h. In the second step, the as-prepared amorphous $RuO_2 \cdot nH_2O$ was heat-treated at 320 °C for 1 h. $RuO_2 \cdot nH_2O$ nanosheets were derived from the hydrolysis process of $RuCl_3 \cdot xH_2O$ under hydrothermal conditions. The formation of RuO_2 nanocrystals involved coalescence of $RuO_2 \cdot nH_2O$ nanosheets, accompanied by chemical bonds breaking and reforming during the sintering process. After heat treatment in a muffle furnace, the morphology of the sample changed from nanosheets to nanoparticles, which is illustrated in **Figure 2**.

2.3. Characterization of RuO_2 Nanocrystals and As-Prepared CEs

Typical scanning electron microscopy (SEM) images (**Figure 3**a,b) show the overall morphology of the amorphous $RuO_2 \cdot nH_2O$ nanosheets and RuO_2 nanoparticles, respectively, from which we can conclude that the sintering process leads to formation of RuO_2 nanocrystals with relatively uniform size. The high-resolution transmission electron microscopy (HRTEM) image of RuO_2 nanocrystals mainly bounded by (110) surfaces is shown in Figure 3c. The lattice spacing of 3.17 Å was highly consistent with the (110) facet of the tetragonal RuO_2 crystal,[25] which is further verified in Figure S2 (see the Supporting Information). To observe the detailed information of the RuO_2 nanocrystal and its film morphology, atomic force microscopy (AFM) imaging analysis was performed. A typical 3D AFM image of RuO_2 film is shown in Figure 3d. The film surface has a very uniform morphology with a root-mean-square roughness (R_q) of 25.567 nm and an average surface roughness (R_a) of 18.562 nm, which

as low as 0.37 eV, which is lower than that on the Pt electrode ($E_a^{des} = 0.39$ eV).[18] The charge density difference was also analyzed to uncover the bond mechanism between I and the surface Ru_{5c} cation at the TS. As shown in Figure 1f, electrons evidently accumulate at I* to form an ionlike I species, and the Ru–I bond bears a typical ionic bond character in which no orbital overlaps exist between the p-orbitalorbital of ionlike I and the d orbital of surface Ru_{5c}. Bader charge

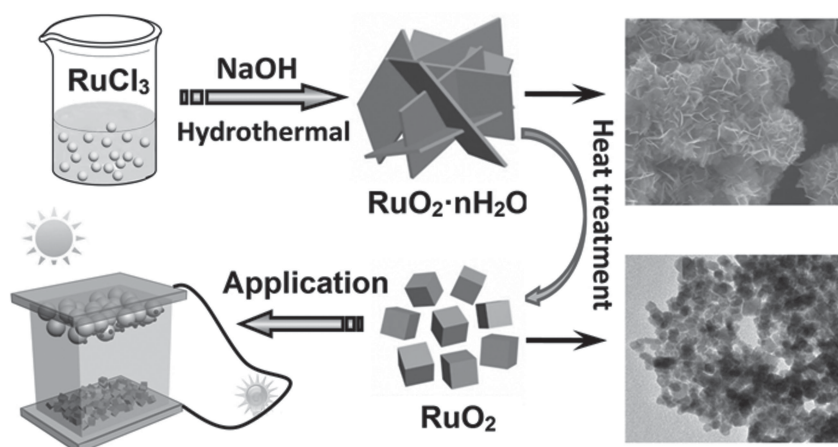© 2013 Wiley-VCH Verlag GmbH & Co. KGaA, Weinheim

Figure 2. Schematic illustration of the synthesis procedure of RuO₂ nanocrystals.

were obtained by analyzing selected line scans across the topology of the RuO₂ film surface (Figure S3). As shown in Figure 3e, all diffraction peaks of the typical X-ray diffraction (XRD) pattern match well with the tetragonal structure of the RuO₂ (space group: $P42/mnm$, JCPDS No. 73–1469). Elemental analysis of these RuO₂ nanoparticles, employing energy-dispersive spectroscopy (EDS; see Figure S4), showed the presence of Ru and O in the sample and a molar ratio of Ru^{4+}/O^{2-} close to 0.5. The particle size distribution, obtained from counting more than 100 individual nanoparticles imaged by SEM, was fairly narrow with an average
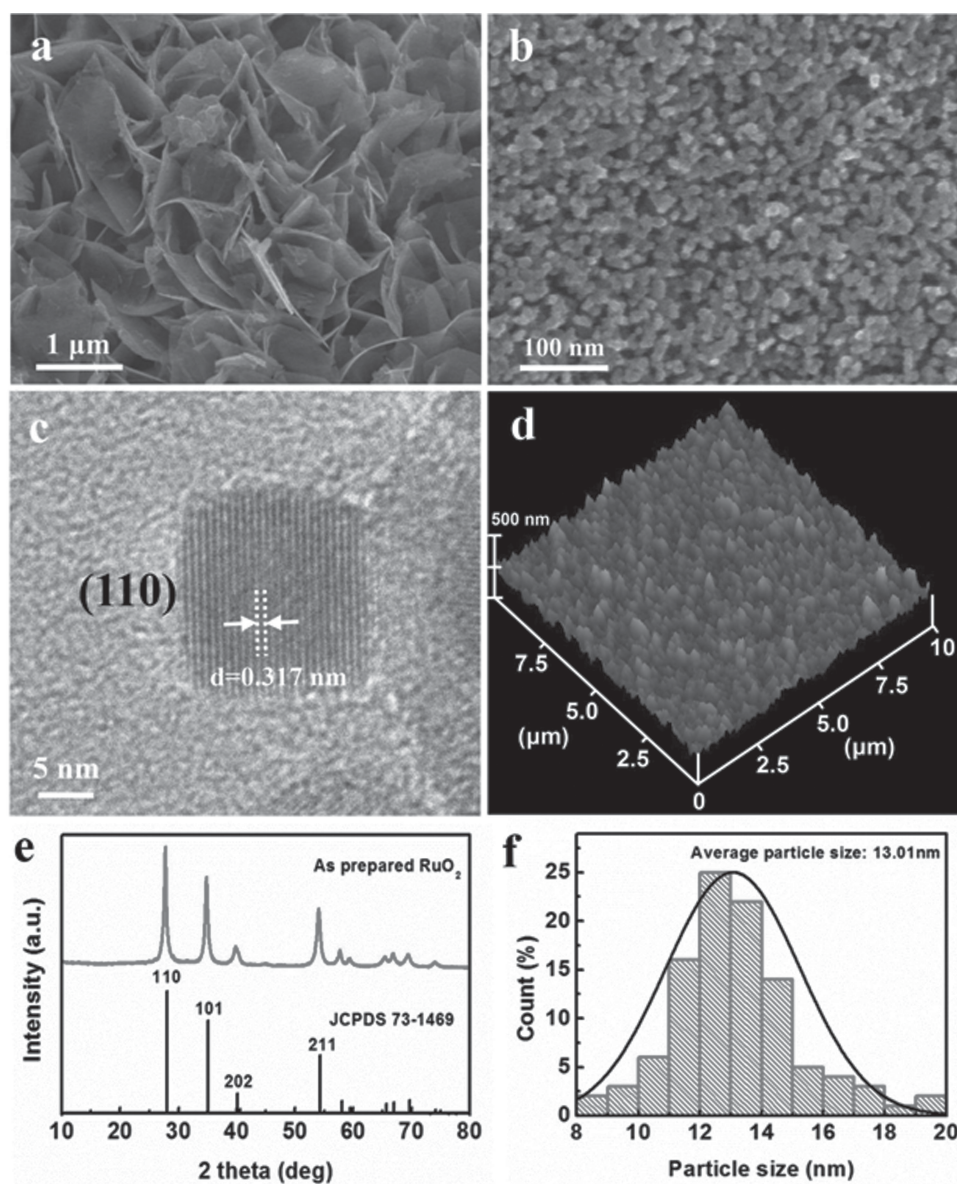

Figure 3. Morphology and crystalline phase determination. a)SEM image of the amorphous RuO₂·nH₂O nanosheets. b) SEM image of the RuO₂ nanoparticles. c)HRTEM image of the RuO₂ nanocrystals. d) Typical 3D AFM image (10 μm × 10 μm) of the as-prepared RuO₂ film. e) Representative XRD pattern of the RuO₂ nanocrystals. f)Size distribution of the RuO₂ nanocrystals in (b).
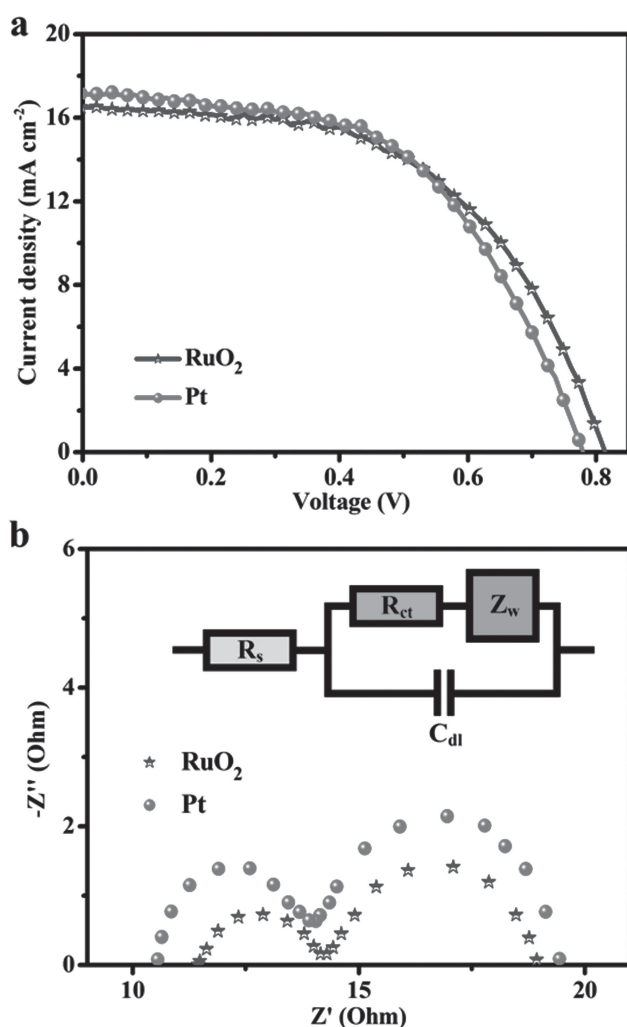
Figure 4. Photocurrent–voltage curves and Nyquist plots from the impedance measurement. a) *J–V* curves of DSCs with RuO_2 and Pt CEs, which were measured in the dark and under illumination of AM 1.5 G, one sun illumination (100 mW cm^{-2}). b) Nyquist plots for the symmetric cells with two identical CEs of RuO_2 or Pt. The corresponding circuit is shown in the inset (see below for definitions).

Table 1. Photovoltaic parameters of DSCs with different CEs[a] and the simulated data from EIS spectra.[b]

CE[c]	J_{sc} [mA cm^{-2}]	V_{oc} [mV]	FF [%]	Eff. [%]	R_s [Ω]	R_{ct} [Ω]	C_{dl} [μF]	E_{pp}[d] [mV]
RuO_2	16.51	813	54	7.22	11.5	2.6	3.6	597
Pt	17.14	778	54	7.17	10.6	3.3	5.5	672

[a]J_{sc}: short-circuit photocurrent density; V_{oc}: open-circuit voltage; FF: fill factor; Eff.: energy conversion efficiency; [b]R_s: series resistance; R_{ct}: charge-transfer resistance; C_{dl}: double - layer capacitance; [c]Thephotocurrent − voltage measurements were carried out under an AM 1.5 G one sun intensity of 100 mW cm^{-2}. During the measurement, the samples were covered with a black mask with an aperture to prevent extra light coming through the lateral space. The active areas of the samples were about 0.250 cm^2 for all of the samples; [d]E_{pp}: the peak-to-peak splitting from CV curves.

comparable to that of DSCs with Pt CEs (7.17%). On the one hand, the J_{sc} (16.51 mA cm^{-2}) for the DSC of RuO_2 CEs is slightly lower than that of Pt CEs (17.14 mA cm^{-2}) owing to the thick film used (see Figure S5), which indicates that RuO_2 CEs show close electrical conductivity to that of Pt CEs.[15] The UV/Vis reflection spectra of RuO_2 and Pt electrodes are shown in Figure S6. The results indicate that the reflective property of the CE film with Pt could improve the light-harvesting efficiency, thus contributing to enhancing the photocurrent.[13] On the other hand, both the electrical conductivity and electrocatalytic activity of CEs can determine the efficiency of DSCs, but the dominant contributions to the high performance of the RuO_2 catalyst reported in this work are owing to the superior electrocatalytic activity. Furthermore, a higher V_{oc} with an improvement of 35 mV was observed after replacing the Pt CE with a RuO_2 CE. The observed difference may be attributed to the more interfacial active sites of RuO_2 CEs and the higher proton concentration in the case of Pt CEs.[13,26] All of these results indicate that RuO_2 CEs possess not only high electrical conductivity to promote the electron translocation, but also excellent electrocatalytic activity to reduce triiodide to iodide.

2.5. Electrochemical Impedance Spectroscopy

To further investigate the electrochemical characteristics of RuO_2 and Pt electrodes, EIS measurements were carried out with symmetric cells fabricated with two identical electrodes (CE//electrolyte//CE) at 20 °C. As shown in Figure 4b, the Nyquist plots illustrate that two semicircles are observed in the high-frequency (left) and low-frequency (right) regions. The equivalent circuit used to fit the experimental EIS data is shown in the inset of Figure 4b. In the modeling circuit used to mimic the EIS setup, the left semicircle of the Nyquist plots is known to be attributable to the CE.[18,27] The high-frequency intercept on the real axis (Z' axis) represents the series resistance (R_s), and the semicircle in the high-frequency region arises from the charge-transfer resistance (R_{ct}). C_{dl} stands for the double-layer capacitance at the electrode/electrolyte interface, which indicates a surface property of the CE materials.[17] Z_w represents Warburg impedance, which arises from mass transport limitations due to diffusion of the triiodide/iodide couple in electrolyte.[16] It is generally

particle size of 13.01 nm and relative standard deviation of 2.18%, as shown in the histogram in Figure 3f. To further confirm the catalytic activity and electrical conductivity of the RuO_2, the as-prepared RuO_2 powder was subsequently used as CE material to fabricate DSCs.

2.4. Photovoltaic Data

Figure 4 demonstrates the photocurrent–voltage (*J–V*) curves for the DSCs and Nyquist plots of electrochemical impedance spectroscopy (EIS) for the dummy cells, and the corresponding photovoltaic parameters are summarized in **Table 1**. As shown in Figure 4a, the photovoltaic characteristics of DSCs based on RuO_2 CEs were short-circuit photocurrent density (J_{sc}) 16.51 mA cm^{-2}, open-circuit voltage (V_{oc}) 813 mV, and fill factor (FF) 0.54, which yielded an overall energy conversion efficiency (Eff.) of 7.22%, remarkably

accepted that R_s is mainly composed of the bulk resistance of CE materials, resistance of fluorine-doped tin oxide (FTO) glass substrate, and contact resistance. Compared with the R_s value of Pt, a relatively close R_s of RuO$_2$ is observed, thus suggesting that CEs with these two catalysts show a similar high electrical conductivity, which is consistent with the tendency of the observed J_{sc}. Moreover, the R_{ct} of RuO$_2$ is 2.6 Ω, and this value is smaller than that of Pt (3.3 Ω) due to the higher electrocatalytic activity on the reduction of triiodide to iodide,[28] which may illustrate why the energy conversion efficiency of DSCs using RuO$_2$ CEs is comparable to that of Pt CEs. From these results, it is apparent that both photocurrent–voltage measurements and EIS results give the same conclusion that the RuO$_2$ CE may be a promising alternative to the conventional Pt electrode in DSCs.

2.6. Electrochemical Behavior

It is well known that cyclic voltammetry (CV) and Tafel polarization measurement are powerful electrochemical characterization methods. **Figure 5**a shows cyclic voltammograms of the RuO$_2$ and Pt electrodes in a three-electrode system. For these two CEs, typical curves with two pairs of oxidation and reduction peaks (O-1/R-1, O-2/R-2) were obtained as reported in the literature.[20] The left pair of redox peaks corresponds to the reaction of Equation (4), whereas the right-hand one corresponds to the reaction of Equation (5).[29]

$$I_3^- + 2e^- = 3I^- \qquad (4)$$

$$3I_2 + 2e^- = 2I_3^- \qquad (5)$$

Because oxidized ions (triiodide) in the electrolyte diffuse to the CE and are finally reduced to iodide on the surface of the CE, the characteristics of peaks (O-1 and R-1) were investigated to further understand the electrocatalytic process of redox mediators on various CEs. As shown in Figure 5a, although the Pt CEs exhibited prominent features from both oxidation (peak at 0.488 V) and reduction (peak at –0.184 V), the RuO$_2$ CEs showed smaller peak-to-peak splitting (597 mV) and higher current densities than that of Pt, thus suggesting that the electrocatalytic activity of RuO$_2$ toward the I$_3^-$/I$^-$ redox reaction was greater than that of the conventional Pt electrode,[20,30] which is comparable to the tendency of the obtained R_{ct}. From the CV results, the crystalline structures of RuO$_2$ can be deduced to have a superior electrocatalytic activity in reducing triiodide, which is in good accordance with the EIS analysis of the DSCs. Figure 5b demonstrates the Tafel polarization curves of the symmetrical cells used in EIS experiments. The anodic and cathodic branches of the RuO$_2$ electrodes show a larger slope than that of Pt, thereby indicating a higher exchange current density (J_0) on the RuO$_2$ catalyst surface, which is also in good agreement with the R_{ct} values obtained from EIS in terms of Equation (6)[13,31]

$$J_0 = RT/nFR_{ct} \qquad (6)$$

where R is the gas constant, T is the temperature, F is Faraday's constant, and n is the total number of electrons
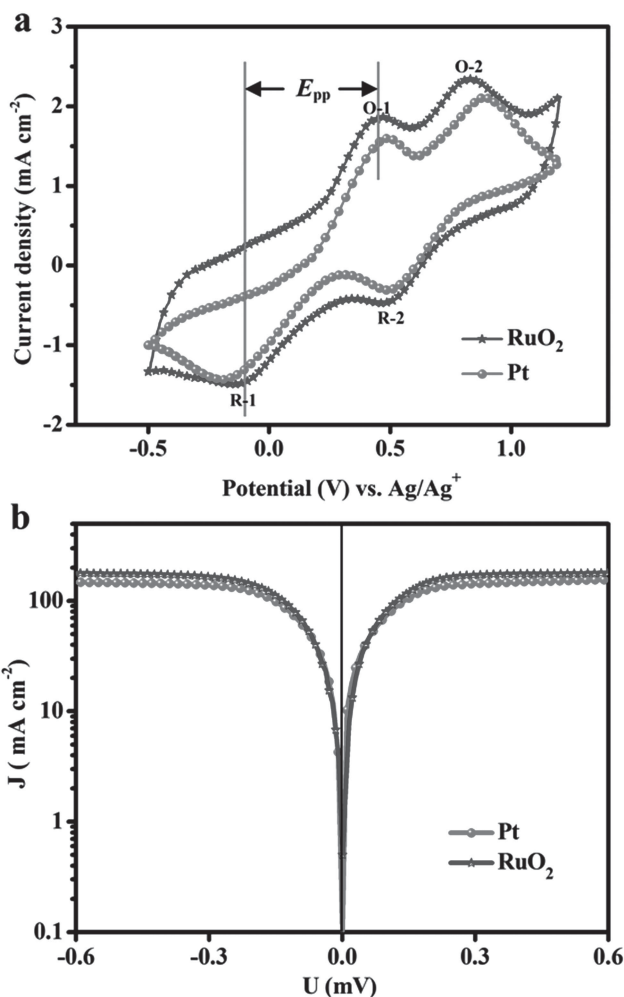

Figure 5. CV and Tafel polarization curves. a) Cyclic voltammogram of triiodide/iodide redox couple for RuO$_2$ and Pt electrodes at a scan rate of 20 mV s^{-1} in 10 mM LiI, 1 mM I$_2$ acetonitrile solution containing 0.1 M LiClO$_4$ as the supporting electrolyte. All measurements were performed in the dark. b) Current–voltage characteristics of the symmetrical (CE//IL//CE) cells fabricated with two identical RuO$_2$ or Pt electrodes at 20 °C.

involved in the electrochemical reduction of triiodide at the electrode. These results demonstrate that the electrochemical triiodide reduction reaction on the RuO$_2$ CEs is comparatively enhanced due to the superior electrocatalytic activity of RuO$_2$ catalyst.

2.7. Electrocatalytic Process and Catalytic Mechanism

After obtaining the basic theoretical and experimental data above, we are in the position to systematically investigate elementary reactions of the electrocatalytic process and understand the catalytic mechanism of electrocatalysis for triiodide reduction on various CEs. Taking the entropies of I$_2$ and I$^-$ in the solvent as well as the chemical potential of an electron under the working voltage into account, the standard Gibbs free energy profile of the IRR occurring at the CH$_3$CN/RuO$_2$(110) interface was calculated. As illustrated in **Figure 6**a, one can see that the I$_2$ dissociation step (½I$_2$(sol) + * → I*) is thermodynamically more favored than that on the
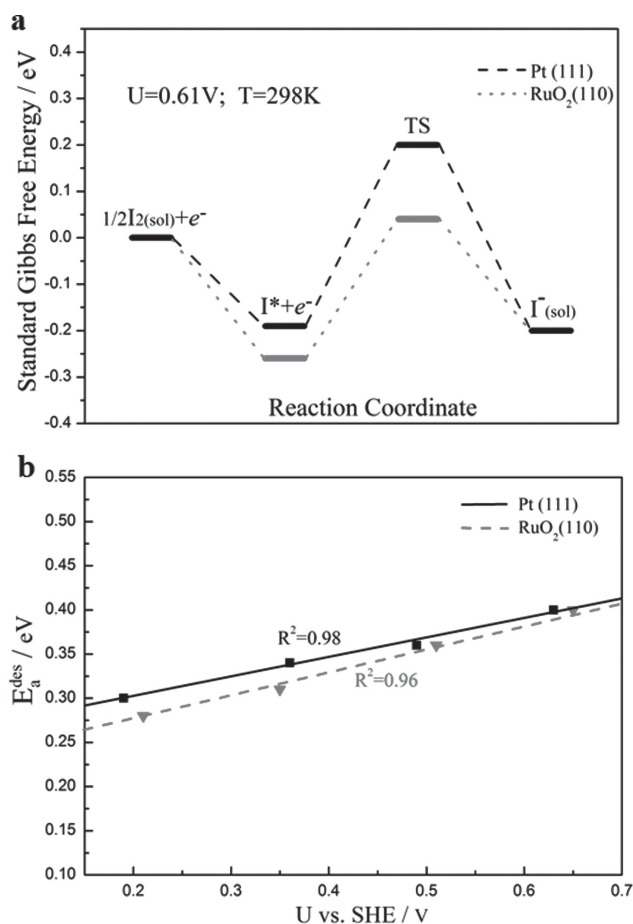
Figure 6. a) Calculated standard Gibbs free energy profiles of the IRR at the CH$_3$CN/RuO$_2$(110) interface. As a comparison, the corresponding Gibbs free energy profile for Pt(111) is also shown. b) Effect of electrode voltage on the desorption barrier. SHE = standard hydrogen electrode.

Pt(111) surface and the I* desorption step also appears relatively easy with a low barrier (0.37 eV), whereas the whole IRR (I$_2$(sol) + 2e$^-$ → 2I$^-$(sol)) process is exothermic by 0.40 eV in terms of the standard Gibbs free energy at room temperature and under the working voltage of 0.61 V. More importantly, this profile is very similar to that at the CH$_3$CN/Pt(111) interface, and there is no evidently high point in the whole profile. Therefore, the high catalytic activity of RuO$_2$ toward the IRR could be expected. Furthermore, we tried a quantitative analysis toward the catalytic activity of RuO$_2$ relative to the Pt electrode. Our previous work indicated that dissociative adsorption of I$_2$ at the CH$_3$CN/Pt(111) interface could be considered to be in equilibrium approximately,[18] whereas at the CH$_3$CN/RuO$_2$(110) interface I$_2$ can readily dissociate and even exhibits a larger adsorption energy relative to Pt(111). Thus, it is believed that I$_2$ dissociation is a fast process on the RuO$_2$(110) surface. From the standard Gibbs free energy profile, it also appears that the relatively difficult step is at the latter I* desorption step. In other words, the overall activity could be mainly determined by the desorption barrier of the I* atom from one-electron reduction. The corresponding barrier of I* at the CH$_3$CN/RuO$_2$(110) interface is 0.37 eV, lower than that (0.39 eV) at the CH$_3$CN/Pt(111) interface, thus

indicating the higher catalytic activity of RuO$_2$(110) relative to Pt(111) in facilitating the IRR, which is consistent with the experimental results.

In addition, considering the importance of E_a^{des} in determining the overall activity, we approximately examined the effect of electrode voltage on the desorption barrier by tuning the system work function (Φ) according to the formula $U = \Phi/e - U_{SHE}$ (see Supporting Information for details).[32] As shown in Figure 6b, a linear relationship between the desorption barrier and the electrode voltage (U) with a small positive slope was achieved on all of these two interfaces. It shows that the desorption barrier goes higher as the electrode voltage increases, although it changes slightly, corresponding to small transfer coefficients. The desorption barrier on the RuO$_2$(110) surface is generally smaller than that on the Pt(111) surface, which accounts for the slightly better performance of the RuO$_2$ electrode.

3. Conclusion

In summary, for the first time, a facile synthesis strategy has been developed to prepare RuO$_2$ nanocrystals by hydrothermal and sintering processes, in which the morphology of the amorphous RuO$_2$·nH$_2$O intermediate changed from nanosheets to nanoparticles. Furthermore, this work demonstrates that the RuO$_2$ nanocrystals could serve as CE materials to obtain a high-efficiency photovoltaic performance (7.22%), which is attributed to the ideal combination of superior electrocatalytic activity and high electrical conductivity. More importantly, the electrocatalytic process of redox mediators on RuO$_2$ catalyst surfaces has been studied in depth by using first-principles calculations, which may offer a promising approach to advancing the insight into the inherent catalysis on the CE materials.

4. Experimental Section

Synthesis of RuO$_2$ Nanocrystals 30 mL: An aqueous solution (30 mL) containing RuCl$_3$·xH$_2$O (0.1311 g) and NaOH (12 g) were placed in a 50 mL beaker, which resulted instantly in a black precipitate suspension. After continuous stirring for 15 min, the suspension solution was transferred into a Teflon-lined stainless-steel autoclave and hydrothermally treated at 180 °C for 48 h. After that the resulting black products were washed thoroughly with 0.5 M HCl solution and deionized water, and then finally dried in a vacuum at 60 °C overnight. The resulting powder was collected and placed in an alumina tube in a muffle furnace. The following parameters were maintained during the thermal treatment: temperature: 320 °C; heating rate: 2 °C min^{-1}; and reaction time: 1 h. After cooling, the prepared RuO$_2$ nanoparticles were collected for further characterization.

Electrode Preparation: The TiO$_2$ was prepared according to the literature.[33] A 12-μm-thick layer of 20 nm TiO$_2$ particles was loaded on fluorine-doped SnO$_2$ (FTO) conducting glass (Nippon Sheet Glass, Japan, 8 Ω square^{-1}) by a screen printing technique. After sintering at 125 °C, the obtained layer was further coated with a 4-μm-thick scattering layer of 200 nm TiO$_2$ particles (HEPTACHROMA, DHS-NanoT200) followed by sintering at 500 °C. After cooling to 80 °C, the two layers of TiO$_2$ films were immersed in

a 5×10^{-4} M solution of N719 dye (Solaronix SA, Switzerland) in acetonitrile/*tert*-butyl alcohol (1:1, v/v) for 24 h. The RuO$_2$ powder was mixed with 2% hydroxypropylmethylcellulose in deionized water and absolute ethanol (5:3, v/v) solution to form a homogeneous paste. A film was then made by the doctor-blading method on a FTO conductive glass. The Pt electrode was prepared by drop-casting 0.5 mM H$_2$PtCl$_6$/ethanol solution on the clean FTO conductive glass. Subsequently, the FTO glass coated with RuO$_2$ or Pt was sintered in a muffle furnace at 450 °C for 30 min and the CEs were obtained.

Fabrication of DSCs: DSCs were assembled together with the dye-sensitized TiO$_2$ electrode and the CE by a 25-µm-thick hot-melt film (Surlyn 1702, DuPont) and sealed by heating. The cell internal space was filled with electrolytes by using a vacuum pump. The liquid electrolyte was composed of 0.60 M 1-butyl-3-methylimidazolium iodide, 0.03 M I$_2$, 0.50 M 4-*tert*-butyl pyridine, and 0.10 M guanidinium thiocyanate with acetonitrile as the solvent. The sealed DSCs were used for photocurrent–voltage tests with an active area of 0.250 cm^2. The symmetrical dummy cells used for EIS and Tafel polarization measurements were assembled by two identical CEs clipping the electrolyte similar to the one used for fabricating the DSCs.

Characterizations and Measurements: The morphology and structure of the samples were characterized by XRD (Bruker D8 Advanced Diffractometer, Cu K$_\alpha$ radiation, 40 kV), HRTEM (Jeol JEM-2010F, F20, 200 kV), and field-emission SEM (Hitachi S4800) with EDS. AFM imaging was also used to analyze the surface topography by using a Dimension Icon scanning probe microscope (Veeco, USA) in the tapping mode. The current–voltage tests of DSCs were performed under one sun conditions using a solar light simulator (Oriel, 91160, AM 1.5 globe). The optical reflection spectra of the samples were recorded in a UV/Vis spectrophotometer (Cary 500). The power of the simulated light was calibrated to 100 mW cm^{-2} using a Newport Oriel PV reference cell system (model 91150 V). The EIS experiments and Tafel polarization curves were measured with dummy cells in the dark by using an electrochemical workstation (Parstat 2273, Princeton). The frequency range of EIS experiments was from 100 mHz to 1 MHz with an ac modulation signal of 10 mV and bias dc voltage of 0.60 V. The curves were fitted by the ZSimpWin software. Tafel polarization measurements were carried out with a scan rate of 50 mV s^{-1}. CV was conducted in a three-electrode system in an acetonitrile solution of 0.1 M LiClO$_4$, 10 mM LiI, and 1 mM I$_2$ at a scan rate of 20 mV s^{-1} by using a BAS 100B/W electrochemical analyzer. Pt served as a CE and the Ag/Ag$^+$ couple was used as a reference electrode.

Supporting Information

Supporting Information is available from the Wiley Online Library or from the author.

Acknowledgements

[1] B. O'Regan, M. Grätzel, *Nature* **1991**, *353*, 737.
[2] A. Hagfeldt, G. Boschloo, L. Sun, L. Kloo, H. Pettersson, *Chem. Rev.* **2010**, *110*, 6595.
[3] M. Wang, S.-J. Moon, M. Xu, K. Chittibabu, P. Wang, N.-L. Cevey-Ha, R. Humphry-Baker, S. M. Zakeeruddin, M. Grätzel, *Small* **2010**, *6*, 319.
[4] J.-H. Yum, E. Baranoff, F. Kessler, T. Moehl, S. Ahmad, T. Bessho, A. Marchioro, E. Ghadiri, J.-E. Moser, C. Yi, M. K. Nazeeruddin, M. Grätzel, *Nat. Commun.* **2012**, *3*, 631.
[5] S. Guldin, P. Docampo, M. Stefik, G. Kamita, U. Wiesner, H. J. Snaith, U. Steiner, *Small* **2012**, *8*, 432.
[6] N. Papageorgiou, *Coord. Chem. Rev.* **2004**, *248*, 1421.
[7] X. Xin, M. He, W. Han, J. Jung, Z. Lin, *Angew. Chem. Int. Ed.* **2011**, *123*, 11943.
[8] R. Bashyam, P. Zelenay, *Nature* **2006**, *443*, 63.
[9] J. E. Trancik, S. C. Barton, J. Hone, *Nano Lett.* **2008**, *8*, 982.
[10] P. Joshi, Y. Xie, M. Ropp, D. Galipeau, S. Bailey, Q. Qiao, *Energy Environ. Sci.* **2009**, *2*, 426.
[11] Q. Li, J. Wu, Q. Tang, Z. Lan, P. Li, J. Lin, L. Fan, *Electrochem. Commun.* **2008**, *10*, 1299.
[12] S. Ahmad, J.-H. Yum, H.-J. Butt, M. K. Nazeeruddin, M. Grätzel, *ChemPhysChem* **2010**, *11*, 2814.
[13] M. Wang, A. M. Anghel, B. t. Marsan, N.-L. Cevey Ha, N. Pootrakulchote, S. M. Zakeeruddin, M. Grätzel, *J. Am. Chem. Soc.* **2009**, *131*, 15976.
[14] H. Sun, D. Qin, S. Huang, X. Guo, D. Li, Y. Luo, Q. Meng, *Energy Environ. Sci.* **2011**, *4*, 2630.
[15] G. R. Li, J. Song, G. L. Pan, X. P. Gao, *Energy Environ. Sci.* **2011**, *4*, 1680.
[16] G.-R. Li, F. Wang, Q.-W. Jiang, X.-P. Gao, P.-W. Shen, *Angew. Chem. Int. Ed.* **2010**, *49*, 3653.
[17] M. Wu, X. Lin, A. Hagfeldt, T. Ma, *Angew. Chem. Int. Ed.* **2011**, *50*, 3520.
[18] Y. Hou, D. Wang, X. H. Yang, W. Q. Fang, B. Zhang, H. F. Wang, G. Z. Lu, P. Hu, H. J. Zhao, H. G. Yang, *Nat. Commun.* **2013**, *4*, 1583.
[19] D.-J. Yun, H.-M. Ra, S. Cho, W. Maeng, S.-H. Lee, S. Park, J.-W. Jang, K. Cho, S.-W. Rhee, *ACS Appl. Mater. Interfaces* **2012**, *4*, 4588.
[20] F. Gong, H. Wang, X. Xu, G. Zhou, Z.-S. Wang, *J. Am. Chem. Soc.* **2012**, *134*, 10953.
[21] I. M. Kodintsev, S. Trasatti, M. Rubel, A. Wieckowski, N. Kaufher, *Langmuir* **1992**, *8*, 283.
[22] Y. S. Hu, Y. G. Guo, R. Dominko, M. Gaberscek, J. Jamnik, J. Maier, *Adv. Mater.* **2007**, *19*, 1963.
[23] A. Hauch, A. Georg, *Electrochim. Acta* **2001**, *46*, 3457.
[24] H. Over, Y. D. Kim, A. P. Seitsonen, S. Wendt, E. Lundgren, M. Schmid, P. Varga, A. Morgante, G. Ertl, *Science* **2000**, *287*, 1474.
[25] J. S. Jirkovský, M. Busch, E. Ahlberg, I. Panas, P. Krtil, *J. Am. Chem. Soc.* **2011**, *133*, 5882.

[26] B. A. Gregg, *Coord. Chem. Rev.* **2004**, *248*, 1215.

[27] F. Fabregat-Santiago, J. Bisquert, E. Palomares, L. Otero, D. Kuang, S. M. Zakeeruddin, M. Grätzel, *J. Phys. Chem. C* **2007**, *111*, 6550.

[28] J. Chen, K. Li, Y. Luo, X. Guo, D. Li, M. Deng, S. Huang, Q. Meng, *Carbon* **2009**, *47*, 2704.

[29] C.-W. Kung, H.-W. Chen, C.-Y. Lin, K.-C. Huang, R. Vittal, K.-C. Ho, *ACS Nano* **2012**, *6*, 7016.

[30] S. S. Jeon, C. Kim, J. Ko, S. S. Im, *J. Phys. Chem. C* **2011**, *115*, 22035.

[31] S. M. Zakeeruddin, M. Grätzel, *Adv. Funct. Mater.* **2009**, *19*, 2187.

[32] J. Rossmeisl, J. K. Nørskov, C. D. Taylor, M. J. Janik, M. Neurock, *J. Phys. Chem. B* **2006**, *110*, 21833.

[33] S. Ito, T. N. Murakami, P. Comte, P. Liska, C. Grätzel, M. K. Nazeeruddin, M. Grätzel, *Thin Solid Films* **2008**, *516*, 4613.